

A novel design for battery cooling based on highly thermally conductive phase change composites encapsulated by 3D printed polyethylene/boron nitride layer

Safna Nishad, Hend M. Elmoughni, Rana Abdul Shakoor, Zawar Alam Qureshi, Buzaina Moossa, Igor Krupa

Item type

Journal Contribution

Terms of use

This work is licensed under a [CC BY 4.0](#) license

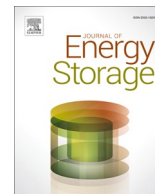
This version is available at

https://manara.qnl.qa/articles/journal_contribution/A_novel_design_for_battery_cooling_based_on_highly_thermally_conductive_r

Access the item on Manara for more information about usage details and recommended citation.

Posted on Manara – Qatar Research Repository on

2025-02-05



Research papers

A novel design for battery cooling based on highly thermally conductive phase change composites encapsulated by 3D printed polyethylene/boron nitride layer

Safna Nishad^a, Hend M. Elmoughni^a, Rana Abdul Shakoor^{a,b}, Zawar Alam Qureshi^a, Buzaina Moossa^a, Igor Krupa^{a,c,*}

^a Center for Advanced Materials, Qatar University, P.O. Box 2713, Doha, Qatar

^b Department of Mechanical and Industrial Engineering, College of Engineering, Qatar University, 2713 Doha, Qatar

^c Materials Science and Technology Graduate Program, College of Arts and Sciences, Qatar University, 2713 Doha, Qatar

ARTICLE INFO

Keywords:

Battery thermal management
Phase change material
Macro-encapsulation
3D printable PE composite

ABSTRACT

Lithium-ion batteries are vital in advancing the cell phone and automotive industry. However, their susceptibility to self-heating impacts their performance, service life, and safety. Thus, efficient thermal management devices are indispensable. Phase change materials (PCM) are increasingly studied for battery thermal management due to their passive thermal storage capacity and temperature homogeneity. However, challenges such as low thermal conductivity and PCM leakage during solid-liquid phase transition limit their applicability. This study presents a novel approach to address these issues by fabricating a highly conductive macro-encapsulated phase change composite. The composite is formed by infiltrating paraffin wax (PW) into graphite foam (GF) and encapsulating it with a polyethylene-boron nitride (PE/BN) composite using 3D printing. The resulting encapsulated GF/PW composite demonstrates excellent thermal properties crucial for efficient battery cooling: thermal conductivity ranging from 4.5 to 4.6 W/m. °C and latent heat 129.5 to 153.1 J/g, respectively. A battery cooling pack (BCP), designed as a hollow cylindrical structure, effectively manages individual lithium-ion batteries' thermal performance without any PW leakage. Tests conducted at various discharge rates show that PCM-cooled batteries achieve significantly lower temperatures than those cooled by natural convection, with a notable temperature reduction of 11.3 °C at a discharge rate of 2.9C. The proposed BCP offers customization through paraffin waxes with varying melting points to adapt to different operational conditions, and its flexible fabrication technique accommodates batteries and battery modules of various sizes and shapes.

1. Introduction

The transportation sector is undergoing a crucial transition towards electric vehicles (EVs) as part of its commitment to environmental sustainability and climate change mitigation. Lithium-ion batteries (LiBs) have emerged as a preferred choice for electric power storage and utilization owing to their high energy density, round-trip efficiency, and lifecycle. However, the performance and safety of LiBs are inherently linked to their operating temperature, posing significant challenges such as thermal runaway risks due to overheating [1,2]. Consequently, effective thermal management systems are indispensable for optimizing battery performance and ensuring safety [3,4].

Battery thermal management systems (BTMS), aimed at regulating

battery temperature within the optimal range, represent a prominent area of research [5,6]. Air cooling is the prevalent method for battery cooling, yet it exhibits drawbacks such as non-uniform cooling and increased battery power consumption [7,8]. Liquid cooling and heat pipes represent alternative BTM approaches, albeit demanding costly structural integration and energy expenditure [9,10]. Conversely, phase change materials (PCM) offer an effective solution by absorbing excess heat and maintaining temperatures at their phase change points. This phenomenon results in efficient thermal regulation with little to no energy consumption [11–13]. The PCMs must possess high thermal conductivity, heat storage capacity, and shape stability to achieve effective thermal management. Additionally, they should be electrically insulating, prevent liquid PCM leakage, and allow for a straightforward

* Corresponding author at: Center for Advanced Materials, Qatar University, P.O. Box 2713, Doha, Qatar.

E-mail address: igor.krupa@qu.edu.qa (I. Krupa).

<https://doi.org/10.1016/j.est.2025.115490>

Received 5 September 2024; Received in revised form 29 December 2024; Accepted 20 January 2025

Available online 5 February 2025

2352-152X/© 2025 The Authors. Published by Elsevier Ltd. This is an open access article under the CC BY license (<http://creativecommons.org/licenses/by/4.0/>).

fabrication process.

Paraffin wax (PW) has gained extensive attention as a PCM due to its high heat capacity, cost-effectiveness, widespread availability, remarkable chemical and thermal stability, non-corrosive nature, and compatibility with various materials, making it versatile and ideal for large-scale thermal energy storage applications [14,15]. However, its intrinsic low thermal conductivity necessitates the incorporation of conductive fillers or foams to enhance performance. The literature documents numerous approaches for improving PW's thermal conductivity, including integration with materials such as graphite [16–18], copper [19–21], aluminum [22,23], and nickel [24,25]. Among these, conductive foams exhibit superiority over fillers due to the formation of conductive networks within the composite [15,25,26]. On the other hand, thermal resistances introduced by the PCM and conductive fillers, coupled with the formation of suboptimal conductive networks, often limit the application of conductive fillers for thermal conductivity enhancement [16,27].

While PW-infiltrated conductive foams demonstrate commendable thermal conductivity and thermal energy storage density, they are plagued by a significant drawback: PW leakage during the phase change process [15,25]. In response to this challenge, polymer-blended PCMs have emerged, with polymers serving as a supporting matrix to prevent PW leakage [28–30]. Although, for such polymer-blended shape stabilized phase change composites (PCCs), conductive fillers are added to enhance the thermal conductivity, the presence of thermal resistances induced by both the fillers and other components often impedes significant conductivity improvement. Furthermore, adding components designed to prevent leakage and enhance thermal conductivity may inadvertently reduce heat storage capacity by decreasing the mass fraction of PCM in the composite [31,32].

The encapsulation of PCMs at micro and macro levels is an efficient technique for preventing leakage, provided careful consideration is given to thermal conductivity and heat storage capacity [33–35]. Macro-encapsulation methods include enclosing PCMs or PCCs within containers of fixed shapes [36,37] or via epoxy coatings [38–40]. For instance, Shang et al. [41] successfully fabricated modularized PCC blocks utilizing PW-infiltrated metal foams with an additional cast-molded epoxy coating, effectively preventing PCM leakage. In their previous study, Nishad et al. [42] encapsulated PW-infiltrated graphite foam using epoxy modified with EG to prevent leakage. This encapsulated material was then utilized for the thermal management of photovoltaic panels. However, casting epoxy coatings for complex shapes necessitates molds and proves challenging for specific applications.

In BTM applications, PCCs play a crucial role in improving thermal conductivity and preventing PCM leakage—for instance, Ma et al. [43] incorporated EG and copper nanoparticles into PW, which they then utilized to fill battery enclosures. However, issues like filler segregation, settlement, and the need for additional encasement remain significant limitations in such systems. Integrating polymers into PCM-filler composites offers a solution to address these challenges, providing shape stability [44–46]. Molefi et al. [47] investigated the PCCs comprising HDPE and LDPE blended with PW, and their findings revealed that paraffin wax can be uniformly dispersed within the polymer matrix. Although polymers like polyethylene octene co-elastomer (POE) [48,49], ethylene-vinyl acetate (EVA) [50], olefin block co-polymer (OBC) [28], and thermoplastic styrene-based polymer (TPS) [51] offer advantages such as flexibility, ease of mold fabrication, and reduction of thermal resistance between batteries and PCM, their thermal conductivity typically remains limited to 0.4–1.8 W/m.K. Additionally, despite maintaining shape stability, these systems are susceptible to PCM leakage, which poses a significant challenge in their practical application. Cao et al. [22] fabricated a composite of PW, EG, carbon fiber, and HDPE, which they integrated into a 3D-printed aluminum honeycomb structure featuring fins. This innovative design yielded a remarkable thermal conductivity of 5.723 W/m.K. and effectively controlled maximum battery temperatures, ensuring they remained below 45.5 °C

even during discharge rates of 2.5C. However, the complexity of the fabrication technique and higher electrical conductivity pose challenges for its application to battery packs of varying dimensions. Thus, there is a pressing need for highly conductive, leak-proof, and easily implementable fabrication techniques for BTM systems employing PCMs.

The widespread adoption of 3D printing in recent years has revolutionized the fabrication of complex geometries [22,52–54]. Advances in 3D printing technology now enable the printing of functional composites using polymers like PLA [55–57] and ABS [58–60]. This progress opens up new avenues for preparing coatings suitable for intricate geometries. Considering factors such as cost and availability, polyethylene emerges as a promising material for 3D printing [61–64]. Moreover, various techniques for functionalizing polyethylene to enhance its thermal conductivity further contribute to its suitability for coating applications.

While functional PE composites in the literature have focused on improving thermal conductivity using fillers like expanded graphite [65,66] and carbon fillers [67,68], these additives also enhance electrical conductivity, which is undesirable for BTM applications. Consequently, materials such as boron nitride (BN), with higher thermal and lower electrical conductivity, emerge as more suitable fillers [69–71]. Thermal conductivity remains paramount even for coating applications, as coatings may otherwise diminish the overall thermal conductivity of the composite.

Moreover, despite the advantages of functionalized polymers in addressing shortcomings like shrinkage, warpage, and lower bed adhesion in PE 3D printing [72,73], their application for macro-encapsulation (hereafter termed encapsulation) of PCCs is introduced in this study. This innovative approach aims to optimize both the manufacturing process and the performance of PCCs, contributing to advancements in BTM technology. This work presents a pioneering and creative approach in the field, introducing a novel encapsulated PCC tailored for BTM applications (named battery cooling pack, BCP). While previous studies on PCCs in BTM have struggled to achieve high thermal conductivity and heat storage capacity without PCM leakage, the proposed structure meets these requirements. It features a simple fabrication technique with customization potential to accommodate various battery sizes and shapes at different operational conditions. The BCP facilitates faster dissipation of excess heat during battery operation thanks to its superior thermal conductivity and heat storage capacity over multiple operational cycles. The methodology involves encapsulating PW-infiltrated graphite foams (i.e., GF_PW composite) with 3D-printed PE/BN composites optimized explicitly for 3D printability and enhanced thermal conductivity. The battery cooling packs are fabricated into hollow cylindrical shapes designed to encase LiB 18650 cells, facilitating testing of their thermal management efficacy. Notably, 3D printing for the PE/BN composite eliminates complex molds typically required for epoxy casting, streamlining the manufacturing process. Although battery module testing is not conducted in this study due to limitations in battery tester availability, individual 18650 LiB batteries are tested at various discharge rates to assess the impact of two different GF_PW composites featuring distinct phase change temperatures.

2. Experimental

2.1. Materials

Two grades of paraffin waxes (RT35 and RT44 with melting points of 35 °C and 44 °C, respectively, these PWs were selected based on our previous study on thermal management of solar panels [42]) were purchased from Rubitherm Technologies, Germany; SGL Carbon GmbH, Germany, provided graphite foam (GF). The GF has a density of 0.075 g/cm³ and a thickness of 15 mm. The linear low-density polyethylene (LLDPE) of density 0.93 g/cm³ was supplied by Qatar Petrochemical Company, QAPCO, Qatar. The hexagonal boron nitride (BN) particles of 35 µm were purchased from Itowu Dalian Trading Company, China.

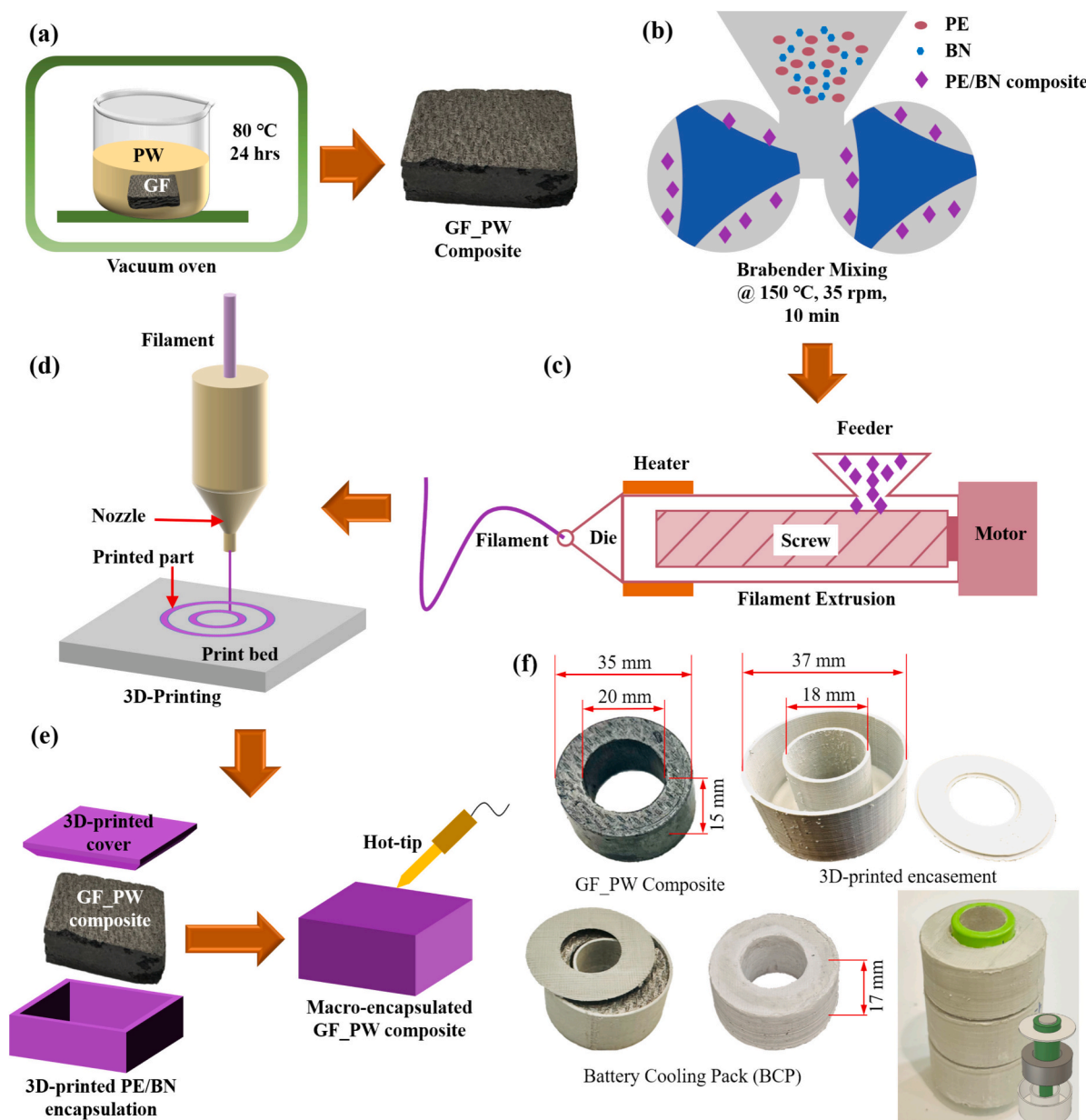


Fig. 1. Fabrication process of Battery cooling Pack (BCP): (a) GF_PW composite preparation, (b) melt-blending of the encapsulating PE/BN composite, (c) filament extrusion of PE/BN composite, (d) 3D printing, (e) encapsulation of GF_PW composite for different characterization, and (f) The Battery cooling pack for BTM study.

2.2. Preparation of GF_PW composite

The GF_PW composites were created using a vacuum impregnation method. Initially, the PW was melted at 70 °C. The GF was then fully submerged in the molten PW and placed in a vacuum oven, where it was maintained at 50 kPa for 24 h (Fig. 1a). The impregnation temperature was set at 70 °C to ensure optimal viscosity for PW penetration into GF foams while preventing PW evaporation at higher temperatures. The impregnation time was also chosen to streamline the process while maximizing PW content. After 24 h of impregnation, the GF_PW composites were carefully removed from the oven while still above the melting point of PW. Any excess wax on the sample was cleaned off using cotton tissue. The PW content in the GF_PW composites was determined by weighing the composites before and after the impregnation process to calculate the mass difference. These gravimetric measurements revealed a PW content of approximately 85–86 % within the GF_PW composite.

2.3. Preparation of PE/BN composite

The PE/BN composite was prepared by blending LLDPE with BN in a melt mixer (Brabender® Plastograph®, Germany) at 160 °C for 15 min (Fig. 1b). Composites with three different mass fractions of BN (i.e., 20, 30, and 40 wt% of BN) were prepared and characterized to select the optimum composite with high thermal conductivity and better 3D printability. The composite was then extruded into filament using a bench-top single-screw extruder Felfil filament maker (Felfil SRL, Italy) at 160 °C, as shown in Fig. 1c. The diameter of the extruded filaments was kept at 1.9 ± 0.05 mm, by controlling both the rotation and drawing speeds. Next, the prepared filaments underwent 3D printing using a dual nozzle Flashforge FDM printer (Creator Pro 2 from Flashforge, USA) (Fig. 1d). This was done to generate a variety of 3D printed components for encapsulation of GF_PW composites, varying in shapes and sizes to facilitate diverse characterization and testing purposes as shown in Fig. 1e and f.

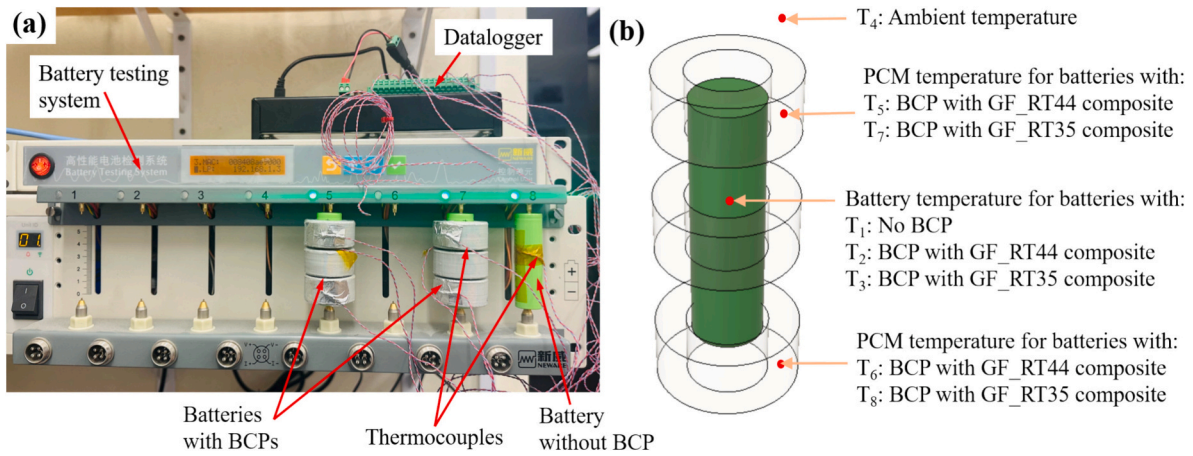


Fig. 2. (a) Photographic view of the BTM test setup and (b) schematic of the thermocouple placement in the BTM test setup.

2.4. Encapsulated GF_PW composites

The GF_PW composite was encased in a 3D printed structure prepared using optimized PE/BN composite to avoid liquid PCM leakage, as shown in Fig. 1f. Different sizes of GF_PW composite samples with and without encapsulation are used for various characterization; (i) $20 \times 20 \times 15$ mm size for quantifying the PW leakage before and after encapsulation, (ii) $30 \times 35 \times 17$ mm size for measuring heat storage capacity and thermal conductivity of the encapsulated GF_PW composite in a homemade transient guarded hot plate (TGHP) apparatus, and (iii) hollow cylindrical shape for BTM study (BCP).

For BCP preparation, hollow cylindrical units of GF_PW composites and 3D-printed PE/BN encasement are prepared as per the dimensions shown in Fig. 1f. The GF_PW composite was manually cut from the parallelepiped composite sample and then inserted into the encasement, covered with a 3D-printed top cover, and firmly secured in place via melt-fusion using the hot-tip technique. The resulting section of the BCP is 18 mm inside diameter, 37 mm outside diameter, and 17 mm height. Three such units were employed to accommodate a Li-Ion battery with dimensions of 18 mm diameter and 65 mm length (MP-18650, 3.7 V, 2.5 Ah).

2.5. Characterization

The GF, GF_PW composite morphology, and encasing PE/BN composite was analyzed using a Nova Nano SEM 450 scanning electron microscope operating at 5 kV. To evaluate the phase-change behavior of the RT35, RT44, GF_RT35, and GF_RT44 samples, differential scanning calorimetry was performed with a DSC 214 Polyma (NETZSCH-Gerätebau GmbH, Germany). The DSC analysis was conducted at a heating/cooling rate of $10^\circ\text{C}/\text{min}$ within a nitrogen atmosphere. The GF_RT35 composite underwent 75 cycles to assess thermal cycling under the same DSC conditions. The thermal stability of RT35, RT44, GF_RT35, GF_RT44, and PE/BN composites was analyzed through thermogravimetric analysis (TGA) using a TGA 4000 (PerkinElmer, USA) analyzer. The samples were heated from ambient temperature to 600°C at a rate of $10^\circ\text{C}/\text{min}$ in a nitrogen atmosphere.

Gravimetric measurements were performed on $20 \times 20 \times 15$ mm samples of the GF_PW composites with and without encapsulation. The samples were placed in an oven set to 70°C for two weeks, and their mass was measured with an analytical balance. The mass loss was then computed using the formula provided in Eq. (1):

$$\text{Mass loss (\%)} = 100 - \frac{(m_i - m_f)}{m_i} \times 100, \quad (1)$$

where m_i is the initial mass of the specimen, m_f is the actual mass of the

specimen after two weeks in the oven, and w is the mass fraction of PW in the composite.

The manufacturer provided the thermal conductivity of the PWs. In contrast, the thermal conductivities of GF, GF_PWs, and PE/BN composites were measured using a thermal constant analyzer (TCA) with a transient plane source at a temperature of 21°C (TPS 2500, Hotdisk, Sweden) with an accuracy of $\pm 3\%$. The thermal conductivity of the encapsulated GF_PW composite was predicted using the series-parallel model introduced by Shang et al. [74]. This model treats the composite as comprising constituent layers arranged in series and parallel. The effective thermal conductivity is calculated based on the volume fractions and thermal conductivities of the individual layers, as described by Eq. 2 [74]:

$$\lambda_{\text{eff}} = \frac{h_1 - h_2}{h_1} \lambda_{\text{PE/BN}} + \frac{h_2}{h_1} \left(\frac{w_1 l_1 - w_2 l_2}{w_1 l_1 \lambda_{\text{PE/BN}}} + \frac{w_2 l_2}{w_1 l_1 \lambda_{\text{GF_PW comp}}} \right)^{-1} \quad (2)$$

where λ_{eff} , $\lambda_{\text{PE/BN}}$, and $\lambda_{\text{GF_PW comp}}$ are the effective thermal conductivities of the encapsulated GF_PW composite, PE/BN composite, and the GF_PW composite, respectively; w_1 , l_1 and h_1 are the width, length, and height of the encapsulated GF_PW composite, respectively; and w_2 , l_2 , and h_2 are the width, length, and height of the GF_PW composite, respectively.

The TGHP apparatus also estimates the encapsulated GF_PW composites' thermal conductivity and heat storage capacities according to ASTM E1530 and ASTM C1784 recommendations. The detailed procedures are given in Section 3.4.

2.6. Battery thermal management experiment

Fig. 2 provides a photographic view of the experimental setup utilized for assessing the thermal management of the battery. The experimental system consists of three sub-systems: (1) batteries and BCPs, (2) the battery charge-discharge testing system (BTS-4008-5V6A-8, Neware Control Unit, China), and (3) 8 T-type thermocouples and data acquisition system (CR1000X datalogger, Campbell Scientific, USA).

Fig. 2b shows the temperature measurement locations during the BTM test. T₁-T₃ are used to measure the battery temperatures of the reference battery, battery with GF_RT44 composite, and battery with GF_RT35 composite, respectively. T₄ measures the ambient temperature, T₅ & T₆ measures the PCM temperature for the GF_RT44 composite, and T₇ & T₈ measures the PCM temperature of the GF_RT35 composite during the BTM experiment.

2.6.1. Protocols for testing

Before starting the BTM test, each battery was conditioned by cycling three times at standard charging and discharging rates provided by the

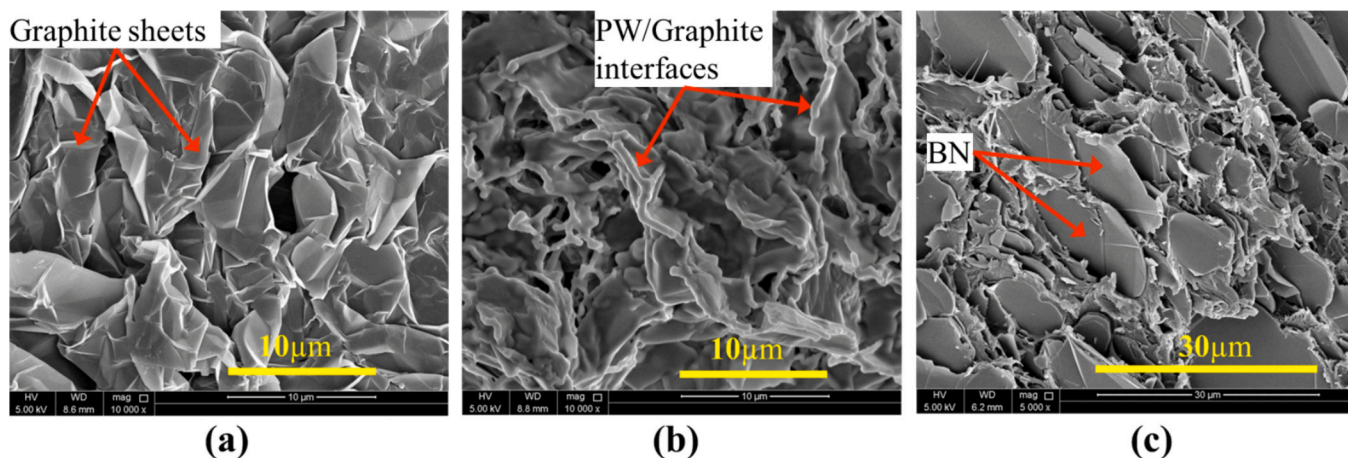


Fig. 3. SEM images of the (a) GF, (b) GF_RT35 composite, and (c) PE/BN composite coating.

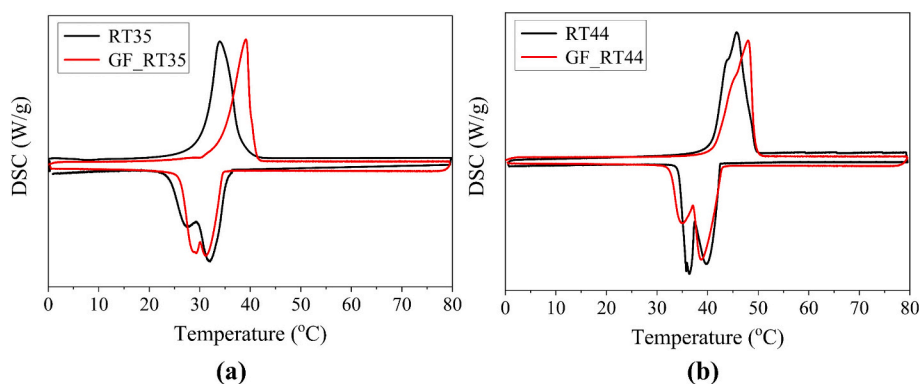


Fig. 4. DSC curves for (a) RT35 and GF_RT35 composite, and (b) RT44 and GF_RT44 composite.

manufacturers (i.e., constant current constant voltage (CC-CV) charging: 1.25 A, with cutoff voltage 4.0 V, 100 mA, constant current (CC) discharge: 1.25 A, with cutoff voltage 2.5 V) to ensure complete formation of solid electrolyte interface and avoid irreversible capacity fading of the batteries. The actual capacities of the batteries are obtained from these tests as 2.5 Ah.

The electrical and thermal performance of the three batteries was tested at different discharge C-rates. The charging operation follows the conventional CC-CV protocol with a 1C charge rate, a cutoff voltage of 4.0 V, and a cutoff current of 0.1 A. A CC protocol was followed for discharge operation with different C-rates (i.e., 1C, 2C, and 2.5C). Each test was conducted for four cycles to understand the cumulative effects of temperature.

3. Results and discussion

3.1. Microstructure of composites

Fig. 3 shows the SEM scans of GF, GF_RT35 composite, and the PE/BN composite used in this study. The micro and macro pores of GF foam, as seen in Fig. 3a, are filled by PW after infiltration, as observed in Fig. 3b. As shown in Fig. 3a, the GF exhibits a highly porous structure created by the interweaving of graphite sheets, resulting in flat and honeycombed configurations with a large specific surface area. The surface tension and capillary forces within the pores facilitate the penetration of liquid PW into the GF, although this can also lead to leakage during operation. The white interfaces visible in Fig. 3b, representing the interaction between PW and the graphite sheets, indicate a high level of wettability, contributing to the formation of a dense GF_PW

Table 1

The phase transition temperatures and latent heat capacities of the PWs and GF_PW composites determined by DSC (the standard deviations for the three samples are shown in parentheses).

Sample	Heating		Cooling	
	T_m (°C)	ΔH_m (J/g)	T_c (°C)	ΔH_c (J/g)
RT35	33.9	227.6 (0.2)	31.8	227.4 (0.1)
GF_RT35	39.1	188.7 (1.6)	31.1	189.4 (1.8)
RT44	45.7	249.0 (0.1)	39.5	247.5 (0.1)
GF_RT44	48.0	209.0 (1.7)	38.7	210.6 (1.5)

composite. The excellent continuity at the interfaces, without any separation, suggests enhanced thermal transport throughout the composite. The uniformly distributed BN particles in Fig. 3c form a three-dimensional conductive network that enhances the thermal conductivity of PE. Moreover, the hexagonal BN particles are aligned in the print direction (Fig. 3c shows the cross-sectional view of the 3D-printed PE/BN composite) and can enhance the thermal conductivity significantly.

3.2. Thermophysical properties of composites

The DSC curves of pure PWs and GF_PWs given in Fig. 4 show their phase transition behavior. The latent heat capacities and phase transition temperatures of RT35, RT44, GF_RT35, and GF_RT44 are shown in Table 1. The DSC analysis of all samples shows a single melting peak and two peaks for the solidification curve. The porous structure of the GF influenced the phase change temperature of the PWs in the composite. As indicated in Table 1, the melting points of the GF_PW composites are

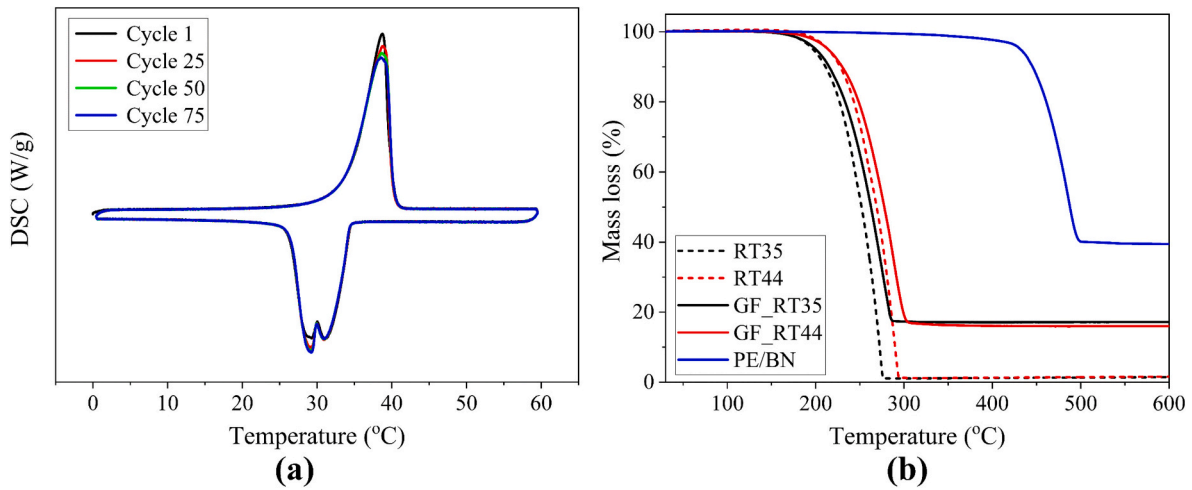


Fig. 5. (a) The DSC thermal cycle curves for GF_RT35 and (b) the TGA curves for the PWs, GF_PW composites, and PE/BN composite.

2.3–5.2 °C higher, and the crystallization peaks are 0.7–0.8 °C lower than their corresponding pure PWs. The shift in the phase transition temperature of the PWs in the pores of GF can be interpreted with the Clapeyron-Clausius equation as shown in Eq. (3) [75].

$$\ln \frac{T_2}{T_1} = \frac{\Delta V}{\Delta H} (P_2 - P_1) \quad (3)$$

where T_1 and T_2 are the phase transition temperature, ΔV , and ΔH are the volume change and enthalpy change during phase transition, and P_1 and P_2 are the ambient pressure during phase transition.

The increase in PW volume within the GF pores during melting causes a higher pressure in pores. It leads to the elevation of the melting point of PW within the GF foam compared to pure PWs [75,76]. Similarly, the crystallization temperature of the GF_PW composite is reduced compared to that of pure PWs due to the decrease in pore pressure associated with a reduction in the PW volume.

The latent heat capacities of RT35, RT44, GF_RT35, and GF_RT44, as determined by DSC analysis, are 227.6, 249, 188.7, and 209 J/g, respectively. The decrease in the latent heat of the composites stems from substituting the heat storage material with GF, which acts as a supportive element for PW and improves its thermal characteristics. Consequently, the thermal energy densities of the GF_RT35 and GF_RT44 composites are 82.9 % and 83.9 % of those of the pure PWs, respectively. The DSC measurements were performed in triplicate, and

the average values, along with the standard deviations for latent heat capacities, are presented in Table 1. Additionally, cyclic DSC analysis involving 75 cycles was carried out for the GF_RT35 composite, as depicted in Fig. 5a, to validate the consistency of the composite's energy storage and release performance. The minimal fluctuations in the phase transition temperature and latent heat demonstrate the stability of the composite even after undergoing extensive thermal cycling.

The thermal stability of PWs, GF_PW composites, and PE/BN composite, as determined by TGA, is depicted in Fig. 5b. The mass loss observed at various temperatures indicates the degradation of different components within the composite, enabling the determination of their respective mass fractions. Accordingly, the amount of PW infiltrated into the GF matrix was inferred from the TGA curve and compared with the results from the DSC analysis. Pure RT35 and RT44 decomposition occur within 165–275 °C and 175–295 °C, respectively. The degradation of RT35 and RT44 within their respective composites persisted up to temperatures of 285 °C and 305 °C. This phenomenon might be attributed to PW being trapped within the micropores of GF, thus retarding the formation and release of volatile by-products during PW's thermal degradation. The mass percentages of PWs in the GF_PW composites were 82.8 % for GF_RT35 and 84 % for GF_RT44. Additionally, the mass fraction of BN in the PE/BN composite was 40 %, as shown in Fig. 5b.

The shape stability of the GF_PW composite is a critical factor in energy storage applications. It was assessed by measuring the PW

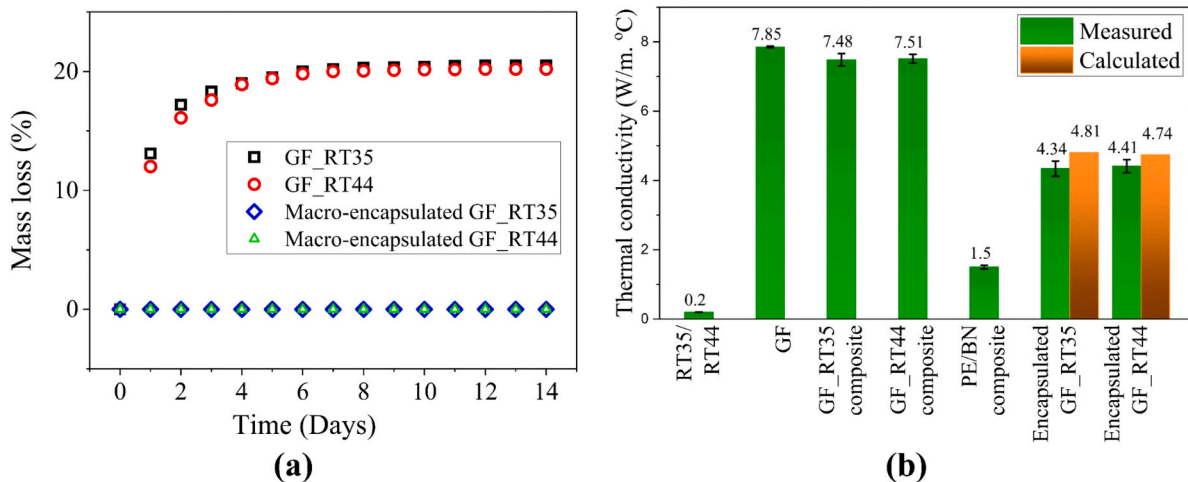


Fig. 6. (a) PW mass loss from the GF_PW composites with and without encapsulation for two weeks and (b) The measured thermal conductivities of the PWs, GF, PE/BN, and GF_PW composites, encapsulated GF_PW composites, and the calculated thermal conductivity of encapsulated GF_PW composites.

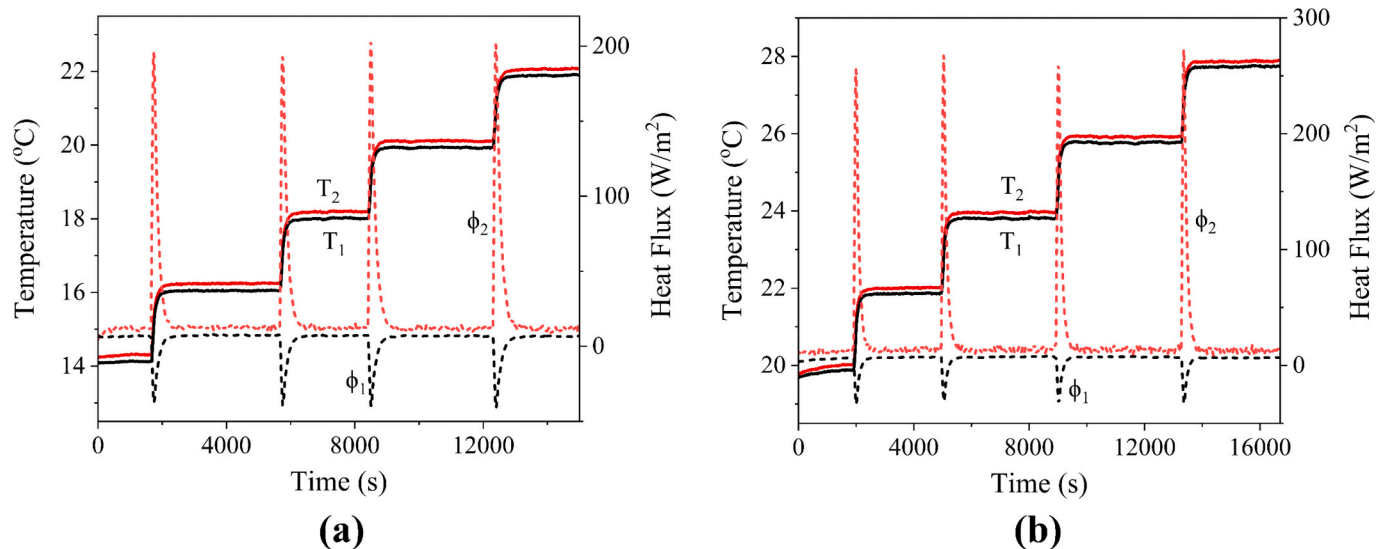


Fig. 7. The temperature and heat flux evolution of the composites in the solid state: (a) encapsulated GF_RT35 (14–22 °C) and (b) encapsulated GF_RT44 (20–28 °C).

leakage from the composite when subjected to temperatures exceeding its melting point. Fig. 6a illustrates the composite's mass loss when subjected to an 80 °C environment for two weeks. GF_PW composites experience a 20 % mass loss without encapsulation over this period. However, the encapsulated GF_PW composite shows no leakage even after exposure to 80 °C for two weeks, demonstrating its excellent thermophysical stability.

3.3. Thermal conductivity

Thermal conductivity is pivotal in determining thermal transfer efficiency in practical applications. Fig. 6b illustrates the thermal conductivity characteristics of various materials, including pure PWs, GF, GF_PW composites, the PE/BN composite, and encapsulated GF_PW composites. The thermal conductivities of homogeneous materials—specifically GF, GF_PW composites, and PE/BN composite—were measured using a thermal constant analyzer (TCA). However, the thermal conductivities could not be determined with the TCA for the encapsulated GF_PW composite, which has a layered structure with

different composites. Instead, they were measured using the TGHP technique, following ASTM E1530 standards.

The encapsulated GF_PW composites, sized at 30 × 35 × 17 mm, are equipped with heat flux sensors and thermocouples on their top and bottom sides. These composites are positioned between two aluminum heat exchangers, as illustrated in Fig. S1 (Supplementary material). The composite samples' thermal resistance and corresponding thermal conductivity under a temperature gradient were computed using Eqs. S1 and S2 (Supplementary material; the detailed procedure can be found in Supplementary material). Table S1 displays the thermal conductivity values for the encapsulated GF_PW composites as determined from the TGHP technique, which is also illustrated in Fig. 6b as the measured values for the corresponding composites (i.e., 4.34 and 4.41 W/m.°C for GF_RT35 and GF_RT44, respectively). Additionally, because of its layered structure, the thermal conductivities of the encapsulated GF_PW composite were calculated using the series-parallel model outlined in Section 2.5. These calculated thermal conductivity values are presented in Fig. 6b as 4.74 W/m.°C for GF_RT35 and 4.81 W/m.°C for GF_RT44 composites. The slightly higher values of calculated thermal

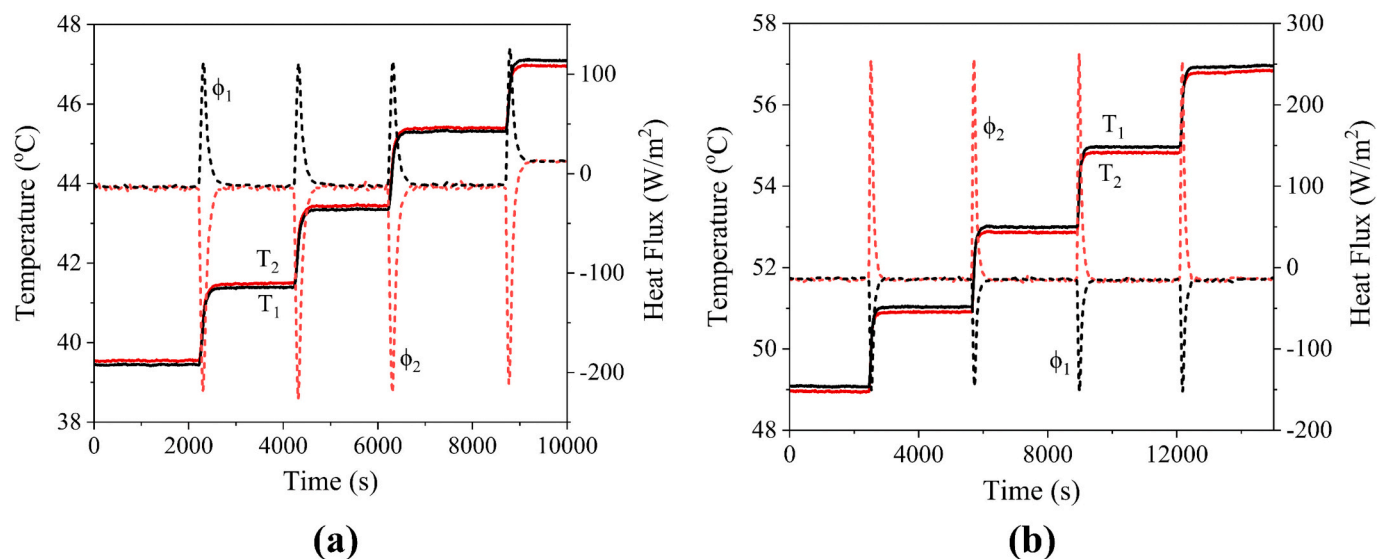


Fig. 8. The temperature and heat flux evolution of the composites in the liquid state: (a) encapsulated GF_RT35 (40–48 °C) and (b) encapsulated GF_RT44 (50–58 °C).

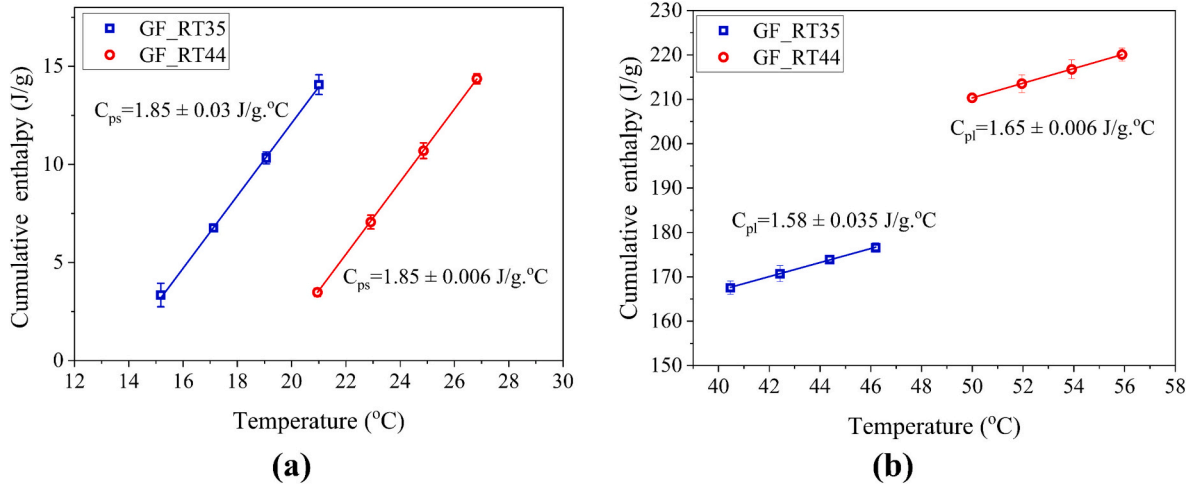


Fig. 9. Specific heat capacities of the encapsulated GF_PW composites as measured by TGHPT: (a) solid-state and (b) liquid-state.

conductivities can be attributed to the series-parallel model's assumption, which overlooks the thermal resistance of the two distinct layers (i. e., GF_PW composite and PE/BN composite encapsulation). This results in overestimating the thermal conductivity compared to the measured values.

The mixing ratio of BN in the PE/BN composite was optimized to enhance thermal conductivity and 3D printability. Thermal conductivity measurements were conducted on various mixtures containing 20, 30, and 40 wt% of BN, resulting in values of 0.98, 1.1, and 1.5 W/m.°C, respectively. It was found that achieving satisfactory 3D printability became challenging beyond 40 wt% of BN. Consequently, a composition comprising 40 wt% of BN in the PE/BN composite was considered optimal for this study.

GF's notably high thermal conductivity, measured at 7.85 W/m.°C, translated into GF_PW composites exhibiting a conductivity 37.5 times greater than pure PWs. However, when GF_PW was encapsulated with the 3D-printed PE/BN composite (i.e., thermal conductivity of 1.5 W/m.°C), the conductivity decreased by a factor of 1.7 compared to GF_PW alone. Nevertheless, the thermal conductivities of the encapsulated GF_PW composites remained significantly higher (22 times) than those of pure PWs.

3.4. The heat storage capacities

3.4.1. The solid and liquid specific heat capacities

DSC was employed to evaluate the thermal performances of the GF_PW composites. However, due to their layered structure, DSC analysis was not feasible for encapsulated GF_PW composite samples. Consequently, the TGHPT analysis was utilized to obtain the thermal performance of the encapsulated GF_PW composites. For TGHPT experiments, parallelepiped samples with dimensions of 30 × 35 × 17 mm were prepared and placed between two aluminum heat exchangers. Throughout the various stages of the experiments, the heat flux and temperature at the samples' bottom and top surfaces were meticulously measured using heat flux sensors and thermocouples. For the detailed procedure, please refer to [77].

To measure the solid C_p , the encapsulated GF_RT35 and GF_RT44 composites were incrementally heated in 2 °C steps, from 14 to 22 °C and 20 to 28 °C, respectively. Similarly, the liquid C_p was determined by subjecting the encapsulated GF_RT35 and GF_RT44 composites to heating from 40 to 48 °C and 50 to 58 °C, respectively. Before each heating step, the samples were held in an isothermal state.

Fig. 7 and Fig. 8 show the temperature and heat flux changes on both sides of the composites for the solid and liquid states, respectively. Heating of the samples was achieved by gradually raising the

Table 2

Thermal properties of the encapsulated GF_PW composites determined by TGHPT analysis.

Sample: Encapsulated composite	Heating			Cooling
	C_{ps} (J/g.°C)	ΔH_m (J/g)	C_{pl} (J/g.°C)	ΔH_c (J/g)
GF_RT35	1.58	129.5	1.85	127.9
GF_RT44	1.65	153.1	1.85	154.0

temperature of both heat exchangers by 2 °C. For each increase in temperature, the heat flux curve displays a peak, and the area under this peak quantifies the energy stored by the composite, which may consist of either sensible heat or a combination of sensible and latent heat, depending on the applied temperature.

The accumulated heat energy at each temperature step was determined using Eq. (4):

$$Q_{\text{stored}} = \frac{1}{\rho \cdot e} \left[\left(\int_{t_{\text{ini}}}^{t_{\text{end}}} (\phi_i - \phi_{eq}) \cdot dt \right) - C_{hft} \cdot \Delta T \right] \quad (4)$$

where e and ρ are the thickness and density of the composite, the area under the peaks of the heat flux curve is indicated by the integral, ϕ_i is the change in the measured heat flux at each time step during an interval dt , ϕ_{eq} is the residual heat flux at the isothermal condition, C_{hft} is the correction factor applied to the heat flux sensor to account for heat storage during the test, and ΔT is the temperature step. The calibration procedure was performed in accordance with ASTM C1784 [78], and the value of C_{hft} was estimated.

Fig. 9 displays the cumulative heat enthalpy at each temperature step plotted against the average of both surfaces' initial and final temperatures. The C_p was determined as the slope of the linear regression line fitted to the data, with an R^2 value exceeding 0.997 [78]. Fig. 9 and Table 2 show the solid and liquid C_p values of the encapsulated GF_PW composites.

3.4.2. The latent heat capacity

Heating and cooling cycles were performed using TGHPT to assess the latent heat storage and release of the encapsulated GF_PW composites. The temperature range for these cycles was 14 to 48 °C for encapsulated GF_RT35 composites and 20 to 58 °C for encapsulated GF_RT44 composites. The energy within the composites comprises both solid and liquid sensible heat and latent heat. Fig. 10 illustrates the heat flux and temperature evolution curves for both types of composites. As

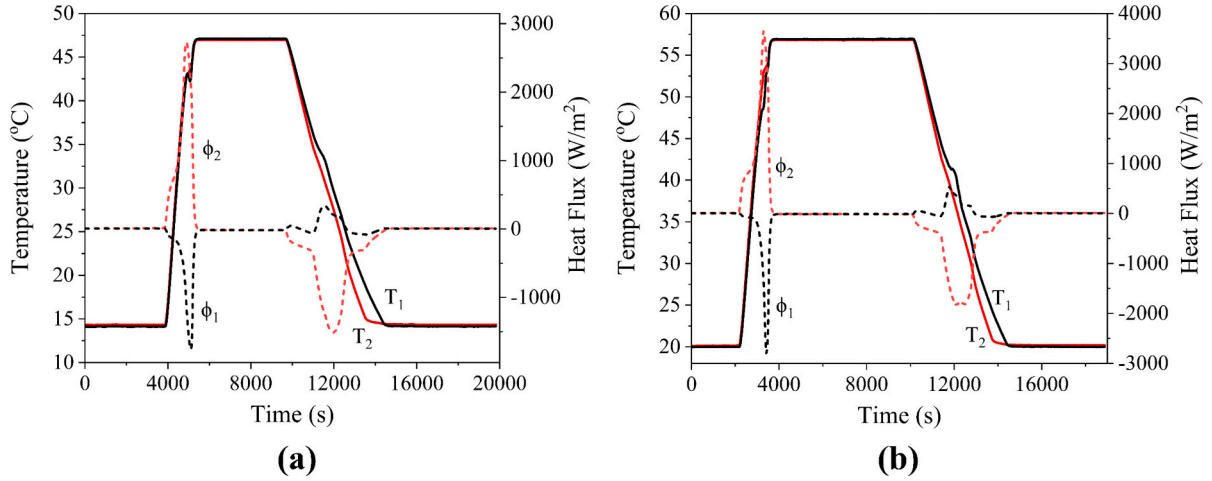


Fig. 10. The temperature and heat flux evolution from solid to liquid for (a) GF_RT35 (14–48 °C) and (b) GF_RT44 (20–58 °C).

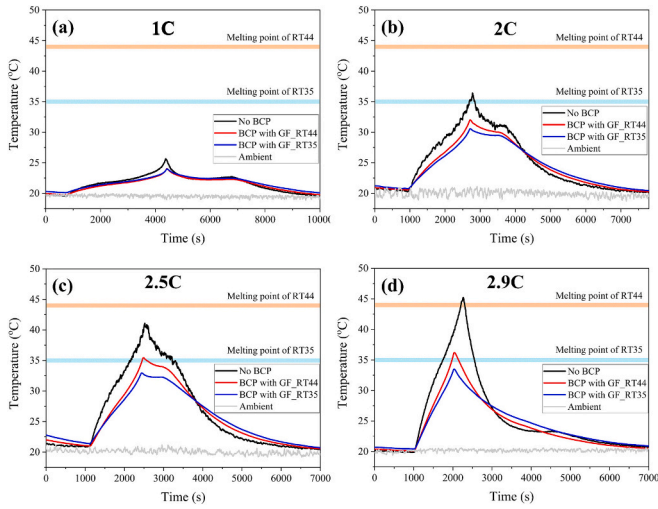


Fig. 11. Temperature evolution of Li-ion batteries without BCP, with encapsulated GF_RT35 and GF_RT44 composites at different discharge rates.

with Figs. 7 & 8, the area under the peaks in Fig. 10 represents the sensible and latent heat stored by the composite during the temperature increase. The total energy stored by the composite can be calculated

using Eq. (4). Sensible heat is subtracted from this total energy to ascertain latent heat, following the method described in Eq. (5).

$$Q_{\text{tot}} = Q_{\text{sens}} + L_m = (C_{ps} \cdot \Delta T_s + C_{pl} \cdot \Delta T_l) + L_m \left(\frac{J}{g} \right) \quad (5)$$

where C_{ps} and C_{pl} are the average specific heat capacities of the material in its solid and liquid states, respectively; ΔT_s and ΔT_l are the temperature changes the material undergoes in its solid and liquid states, respectively; L_m is the latent heat of melting; and Q_{sens} is the sensible heat.

Table 2 presents the average latent heat over three heating and cooling cycles. The sensible heat calculations utilize the estimated C_p values (Table 2), and the precise experimental temperatures. During heating, the PWs are considered solid up to T_m , and during cooling, they remain solid beyond T_c , as outlined in Table 1. The latent heat values were reduced from 188.7 to 129.5 J/g for encapsulated GF_RT35 composites and 209.0 to 153.1 J/g for encapsulated GF_RT44 composites. This reduction results from the addition of PE/BN composite coating, which increases the composite mass without enhancing its heat storage capacity. Consequently, the effective PW loading in the encapsulated composites decreased.

3.5. Battery thermal management study

Fig. 11 illustrates the battery temperature variation at different

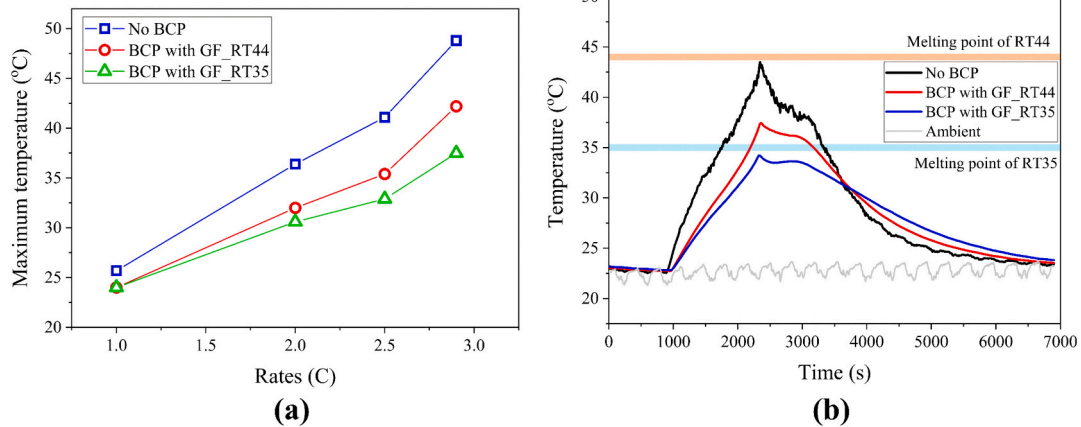


Fig. 12. (a) The variation of the maximum temperature of batteries with and without BCP composites at different discharge rates, and (b) temperature evolution of the batteries with and without BCPS at 2.5C discharge rate and 22.5 °C ambient temperature.

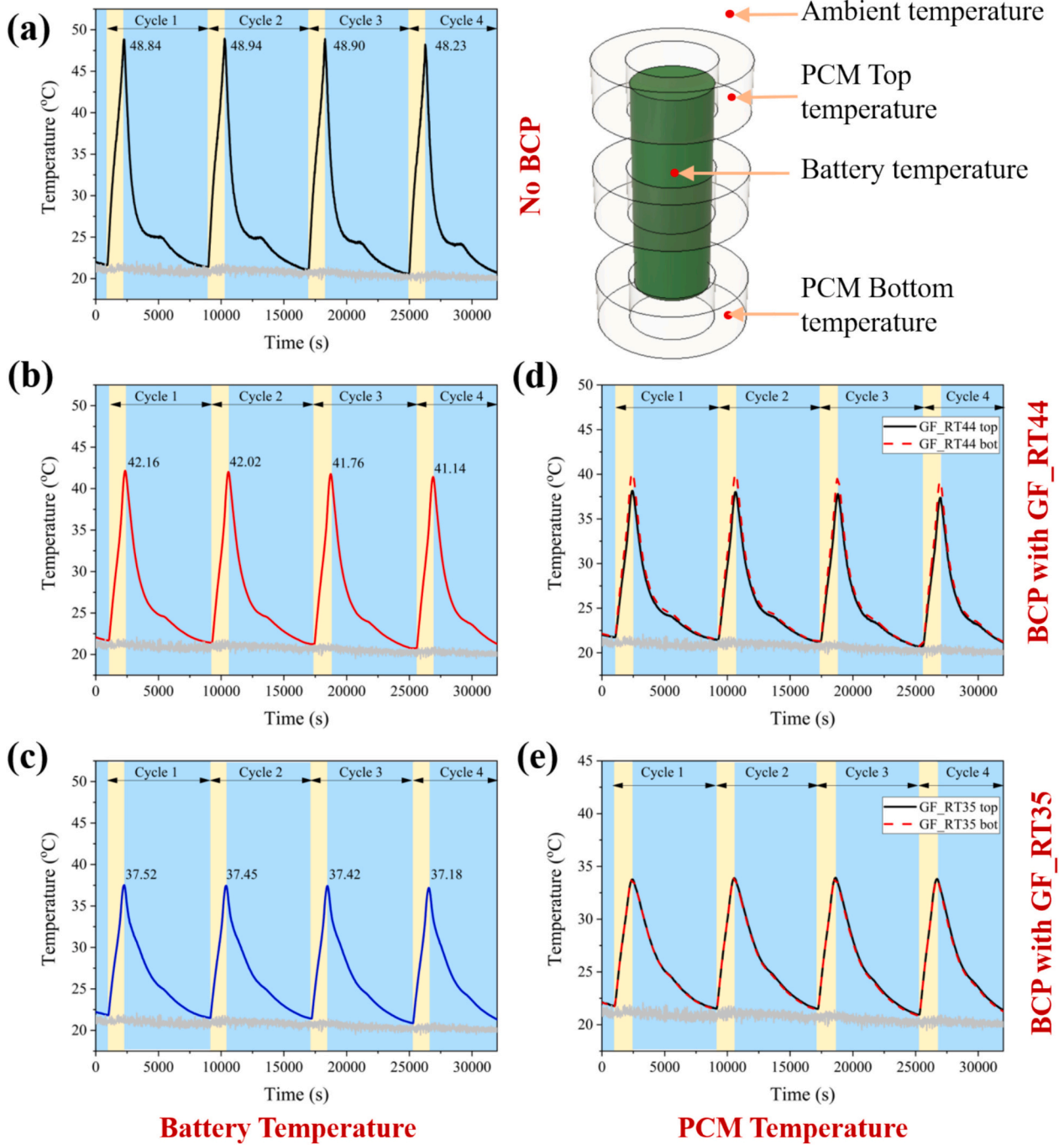


Fig. 13. Battery temperature variation during four cycles of discharge-charge cycles at a discharge rate of 2.9C and charge rate of 1.0C (a) No BCP, (b) BCP with GF_RT44 composite, (c) BCP with GF_RT35 composite, and corresponding PCM temperatures at the top and bottom locations for (d) GF_RT44 composite, and (e) GF_RT35 composite. The grey line represents the ambient temperature.

discharge rates for batteries without BCP and with BCP containing GF_RT44 and GF_RT35 composites. The battery discharge rate is defined as the battery capacity (in Ah) divided by the time taken to discharge, with higher discharge rates indicating quicker draining, also known as rapid discharging. This rapid discharging can lead to the accumulation of internal ohmic heat, which does not have sufficient time to dissipate, resulting in increased battery temperatures. At a 1C discharge rate, the temperature differences among the batteries in the three cases are negligible. However, as the discharge rate increases, the temperature rises at different rates, with the order being No BCP < BCP with GF_RT44 < BCP with GF_RT35 composites. At discharge rates of 2C and 2.5C, the temperature of the No BCP battery increases beyond the

melting range of RT35, and at a 2.9C discharge rate, it reaches the melting range of RT44. This rapid temperature increase is linked to the exponential growth of internal ohmic heat and its inadequate dissipation to the ambient environment. In contrast, the batteries covered with BCPs exhibit a lower heating rate due to the sensible and latent heat storage capacities of the PWs, along with their superior thermal conductivity compared to air in the case of batteries without BCP.

Fig. 12a shows three cases' maximum temperature variation at different discharge rates. The maximum temperature increases from 25.7 °C to 48.8 °C for a battery without BCP at discharge rates of 1C and 2.9C, respectively. However, the corresponding maximum temperatures of batteries with GF_RT44 and GF_RT35 composite BCPs were

Table 3

Comparison of the thermal management performance of PCM-integrated BTM systems reported in the literature and determined in this study.

PCM	Thermal Conductivity (W/m.°C)	Latent heat (J/g)	Reduction in the Battery temperature (°C)	Maximum Battery temperature (°C)	Ref.
Polyethylene glycol/EG/ MXene	1.44	129.7	23.26 %	60	[82]
Polyethylene glycol/EG/ Halloysite nanotube	1.15	103.6	–	47	[83]
PW/EG/styrene-ethylene-butadiene-styrene (SEBS)/ polyethylene octene co-elastomers (POE)	1.29	95.4	11.56	41.5	[84]
Lauric acid/PW/EG	1.22	146.9	–	43.0	[79]
PW/styrene-butadiene-styrene (SBS)/ thermoplastic polyurethane (TPU)/EG	2.52	134.6	–	44.7	[81]
Sodium acetate trihydrate/EG	4.96	181.0	–	52.3	[85]
PW/EG	13.85	249.2	–	42.6	[80]
PW/styrene-ethylene-propylene-styrene (SEPS)/EG	1.34	207.0	–	43	[86]
Lauric acid / SEPS/EG	1.11	111.5	–	46.8	[87]
Polyethylene glycol/Mxene/Ag nanowires	0.64	124.8	12.0	41.9	[88]
Graphite foam+RT35 with 3D-printed PE/BN encapsulation	4.6	153.1	11.3	37.5	This study

24–42.2 °C and 24–37.5 °C, respectively. In other words, integrating BCPs with GF_RT44 and GF_RT35 composites reduced the maximum temperature of the battery by 6.6 °C and 11.3 °C, respectively. The decrease in maximum temperature is less pronounced for the battery with BCP containing the GF_RT44 composite than for the GF_RT35 composite. This is attributed to heat absorption by GF_RT35, which primarily occurs through latent heat storage. As a result, when the battery temperature exceeds the melting point of RT35, the composite effectively absorbs heat at a constant temperature, mitigating temperature growth. In contrast, only a fraction of GF_RT44 contributes to latent heat storage since the maximum battery temperature without BCP barely reaches the melting point of RT44. However, if the discharge rate were increased beyond 2.9C, the battery temperature could surpass the melting point of RT44, allowing the composite to store heat as latent heat and significantly reduce battery temperature. Unfortunately, we could not evaluate the batteries at discharge rates beyond 2.9C due to testing limitations.

However, the consistent increase in maximum battery temperature above ambient levels for each discharge rate suggests the significance of ambient conditions in optimizing PCCs for specific BTM applications (i. e., comparing Figs. 11c and 12b, the ambient temperature and maximum battery temperature differed by 2.5 °C). For instance, in battery applications within higher ambient temperatures, such as 30–35 °C, the GF_RT35 composite proves ineffective because the PCM would already be melted in such conditions, rendering further heat storage impossible for BTM. Conversely, the GF_RT44 composite would be considerably more effective when the maximum battery temperature exceeds the melting point, allowing for latent heat storage. However, this study was limited in conducting experiments at higher ambient conditions due to constraints in the experimental setup. Additionally, as ambient temperature increases further, GF_RT44 may become less effective. Employing higher melting PWs may not adequately address the issue, as allowing battery temperature to exceed 50 °C is not a viable solution for BTM. Therefore, integrating the BCP with liquid cooling systems would provide more effective cooling at a lower energy cost.

The variation in the maximum temperature of the battery with and without BCPs during four charge-discharge cycles is depicted in Fig. 13. Each cycle comprises CC discharge and CC-CV charge modes. As illustrated in Fig. 13a, the battery's temperature reached 48 °C at the end of the discharge process, gradually decreasing to the ambient conditions at the end of CC-CV charging. Meanwhile, the temperature rise of the PCM-based BTM system during discharge mode is reduced due to the heat storage by the PCM as latent heat (Fig. 13b and c). The heightened battery temperature transfers to the BCPs surrounding the battery, leading to a corresponding increase in the PCM temperature, as depicted in Fig. 13d and e. Therefore, it could be inferred that BCPs effectively alleviate the thermal load on batteries during long-term operation, showcasing their potential for BTM systems.

The selection of PCCs depends on the specific application and the maximum operating temperature of the battery in that context. The melting point of the PCM should align with the application's requirements. Infiltrating PCM into highly conductive graphite foam is an improvement over previous methods that utilized expanded graphite fillers for enhancing thermal conductivity for BTM applications [79–81]. Furthermore, encasing the GF_PW composite using PE/BN composite offers three benefits: (i) increasing thermal conductivity, (ii) maintaining lower electrical conductivity, a crucial requirement for BTM applications, and (iii) preventing liquid PCM leakage during operation. Additionally, this study introduces a pioneering approach of encasing PCCs via 3D printing functional polymeric composites, a first in the literature. The thermosetting polymer used for encasement would facilitate improved contact and reduced thermal resistance upon placement of the battery after heating the BCPs due to the enhanced flexibility. Moreover, the BCPs presented in this study exhibit excellence compared to previously reported works, as detailed in Table 3.

4. Conclusions

A novel, highly conductive encapsulated GF_PW composite was successfully fabricated through the infiltration of PW into GF and encapsulation with PE/BN composite using 3D printing. This composite, tailored for battery thermal management, was shaped into a hollow cylindrical form to accommodate individual 18,650 Li-ion batteries as BCPs. The key findings of this study are as follows:

1. The combination of GF_PW composite and PE/BN encapsulation significantly enhanced the thermal conductivity of the encapsulated GF_PW composite to 4.5–4.6 W/m. °C, outperforming PCM composites for BTM reported to date.
2. The encapsulated GF_PW composite exhibited a high heat storage capacity of 129.5–153.1 J/g without PW leakage, indicating excellent thermal stability and reliability.
3. Implementing the BCPs led to a notable reduction in battery temperature across various discharge cycles, achieving a maximum decrease of 11.3 °C compared to natural convection-cooled batteries.
4. The flexible fabrication method allows for customization of the BCPs by using PWs with different melting points, making the technology adaptable to various operating conditions and applications.

These findings underscore the commercial potential of the proposed BCPs, particularly for their customizable design, ease of fabrication, and effective thermal management performance. However, this study was limited to individual batteries tested at an ambient temperature of 20–23 °C. Future research should involve testing the composites on battery packs and under varying ambient temperatures to broaden their applicability. If needed, the BCPs can also be integrated with liquid

cooling systems to manage battery overheating effectively in diverse scenarios at reduced energy costs.'

CRedit authorship contribution statement

Safna Nishad: Writing – original draft, Validation, Methodology, Investigation, Formal analysis, Data curation, Conceptualization. **Hend M. Elmoughni:** Writing – review & editing, Validation, Methodology, Data curation, Conceptualization. **Rana Abdul Shakoor:** Writing – review & editing, Validation, Resources, Methodology. **Zawar Alam Qureshi:** Writing – review & editing, Validation, Methodology. **Buzaina Moossa:** Writing – review & editing, Validation, Methodology. **Igor Krupa:** Writing – review & editing, Validation, Supervision, Resources, Project administration, Methodology, Funding acquisition, Conceptualization.

Funding

This study was funded by the Qatar National Research Fund (a member of The Qatar Foundation), Grant Number NPRP13S-0127-200177.

Declaration of competing interest

The authors declare that they have no known competing financial interests or personal relationships that could have appeared to influence the work reported in this paper.

Acknowledgment

SEM was performed in the Central Laboratories Unit of Qatar University. Open Access funding provided by Qatar National Library.

Appendix A. Supplementary data

Supplementary data to this article can be found online at <https://doi.org/10.1016/j.est.2025.115490>.

Data availability

Data will be made available on request.

References

- [1] P. Liu, C. Liu, K. Yang, M. Zhang, F. Gao, B. Mao, H. Li, Q. Duan, Q. Wang, Thermal runaway and fire behaviors of lithium iron phosphate battery induced by over heating, *J. Energy Storage* 31 (2020) 101714, <https://doi.org/10.1016/J.EST.2020.101714>.
- [2] P. Liu, C. Liu, K. Yang, M. Zhang, F. Gao, B. Mao, H. Li, Q. Duan, Q. Wang, Thermal runaway and fire behaviors of lithium iron phosphate battery induced by over heating, *J. Energy Storage* 31 (2020) 101714, <https://doi.org/10.1016/J.EST.2020.101714>.
- [3] J. Lin, X. Liu, S. Li, C. Zhang, S. Yang, A review on recent progress, challenges and perspective of battery thermal management system, *Int. J. Heat Mass Transf.* 167 (2021) 120834, <https://doi.org/10.1016/J.IJHEATMASSTRANSFER.2020.120834>.
- [4] B. Chidambaramanathan, M. Vijayaraj, V. Suriya, R. Sai Ganesh, S. Soundarraj, A review on thermal issues in Li-ion battery and recent advancements in battery thermal management system, *Mater. Today Proc.* 33 (2020) 116–128, <https://doi.org/10.1016/J.MATPR.2020.03.317>.
- [5] A.G. Mohammed, K.E. Elfeky, Q. Wang, Recent advancement and enhanced battery performance using phase change materials based hybrid battery thermal management for electric vehicles, *Renew. Sust. Energ. Rev.* 154 (2022) 111759, <https://doi.org/10.1016/J.RSER.2021.111759>.
- [6] A. Wazeer, A. Das, C. Abeykoon, A. Sinha, A. Karmakar, Phase change materials for battery thermal management of electric and hybrid vehicles: a review, *Energ. Nexus* 7 (2022) 100131, <https://doi.org/10.1016/J.NEXUS.2022.100131>.
- [7] W. Wu, S. Wang, W. Wu, K. Chen, S. Hong, Y. Lai, A critical review of battery thermal performance and liquid based battery thermal management, *Energy Convers. Manag.* 182 (2019) 262–281, <https://doi.org/10.1016/J.ENCONMAN.2018.12.051>.
- [8] Z. Yu, J. Zhang, W. Pan, A review of battery thermal management systems about heat pipe and phase change materials, *J. Energy Storage* 62 (2023) 106827, <https://doi.org/10.1016/J.EST.2023.106827>.
- [9] C. Hu, H. Li, Y. Wang, X. Hu, D. Tang, Experimental and numerical investigations of lithium-ion battery thermal management using flat heat pipe and phase change material, *J. Energy Storage* 55 (2022) 105743, <https://doi.org/10.1016/J.EST.2022.105743>.
- [10] H. Yang, M. Li, Z. Wang, B. Ma, A compact and lightweight hybrid liquid cooling system coupling with Z-type cold plates and PCM composite for battery thermal management, *Energy* 263 (2023) 126026, <https://doi.org/10.1016/J.ENERGY.2022.126026>.
- [11] C. Liu, D. Xu, J. Weng, S. Zhou, W. Li, Y. Wan, S. Jiang, D. Zhou, J. Wang, Q. Huang, Phase change materials application in battery thermal management system: a review, *Materials* 13 (2020) 4622, <https://doi.org/10.3390/MA13204622>.
- [12] J. Luo, D. Zou, Y. Wang, S. Wang, L. Huang, Battery thermal management systems (BTMs) based on phase change material (PCM): a comprehensive review, *Chem. Eng. J.* 430 (2022) 132741, <https://doi.org/10.1016/J.CEJ.2021.132741>.
- [13] W. Wu, G.F. Smaism, S.M. Sajadi, M.A. Fagiry, Z. Li, M.A. Shamseldin, H. Aybar, Impact of phase change material-based heatsinks on lithium-ion battery thermal management: a comprehensive review, *J. Energy Storage* 52 (2022) 104874, <https://doi.org/10.1016/J.EST.2022.104874>.
- [14] A.R. Bais, D.G. Subbedar, S. Panchal, Critical thickness of nano-enhanced RT-42 paraffin based battery thermal management system for electric vehicles: a numerical study, *J. Energy Storage* 52 (2022) 104757, <https://doi.org/10.1016/J.EST.2022.104757>.
- [15] Y. Zhao, B. Zou, J. Ding, Y. Ding, Experimental and numerical investigation of a hybrid battery thermal management system based on copper foam-paraffin composite phase change material and liquid cooling, *Appl. Therm. Eng.* 218 (2023) 119312, <https://doi.org/10.1016/J.APPLTHERMALENG.2022.119312>.
- [16] Z. Xia, C. Li, H. Yu, Z. Wang, Experimental study of a passive thermal management system using expanded graphite/polyethylene glycol composite for lithium-ion batteries, *Energies* 16 (2023) 7786, <https://doi.org/10.3390/EN16237786>.
- [17] Z. Wang, C. Du, R. Qi, Y. Wang, Experimental study on thermal management of lithium-ion battery with graphite powder based composite phase change materials covering the whole climatic range, *Appl. Therm. Eng.* 216 (2022) 119072, <https://doi.org/10.1016/J.APPLTHERMALENG.2022.119072>.
- [18] X. Zhao, C. Li, K. Bai, B. Xie, J. Chen, Q. Liu, Multiple structure graphite stabilized stearic acid as composite phase change materials for thermal energy storage, *Int. J. Min. Sci. Technol.* 32 (2022) 1419–1428, <https://doi.org/10.1016/J.IJMST.2022.10.003>.
- [19] C. Ma, Y. Zhang, S. Hu, X. Liu, S. He, A copper nanoparticle enhanced phase change material with high thermal conductivity and latent heat for battery thermal management, *J. Loss Prev. Process Ind.* 78 (2022) 104814, <https://doi.org/10.1016/J.JLP.2022.104814>.
- [20] W. Wu, X. Yang, G. Zhang, X. Ke, Z. Wang, W. Situ, X. Li, J. Zhang, An experimental study of thermal management system using copper mesh-enhanced composite phase change materials for power battery pack, *Energy* 113 (2016) 909–916, <https://doi.org/10.1016/J.ENERGY.2016.07.119>.
- [21] W. Situ, G. Zhang, X. Li, X. Yang, C. Wei, M. Rao, Z. Wang, C. Wang, W. Wu, A thermal management system for rectangular LiFePO₄ battery module using novel double copper mesh-enhanced phase change material plates, *Energy* 141 (2017) 613–623, <https://doi.org/10.1016/J.ENERGY.2017.09.083>.
- [22] M. Cao, J. Huang, Z. Liu, The enhanced performance of phase-change materials via 3D printing with prickly aluminum honeycomb for thermal management of ternary lithium batteries, *Adv. Mater. Sci. Eng.* 2020 (2020), <https://doi.org/10.1155/2020/8167386>.
- [23] Y. Azizi, S.M. Sadrameli, Thermal management of a LiFePO₄ battery pack at high temperature environment using a composite of phase change materials and aluminum wire mesh plates, *Energy Convers. Manag.* 128 (2016) 294–302, <https://doi.org/10.1016/J.ENCONMAN.2016.09.081>.
- [24] A. Hussain, I.H. Abidi, C.Y. Tso, K.C. Chan, Z. Luo, C.Y.H. Chao, Thermal management of lithium ion batteries using graphene coated nickel foam saturated with phase change materials, *Int. J. Therm. Sci.* 124 (2018) 23–35, <https://doi.org/10.1016/J.IJTHERMALSCI.2017.09.019>.
- [25] L. Zhang, J. Zhang, G. Zhang, R. Hu, L. Jiang, Z. Dai, Y. Wen, D. Shao, Experimental study of novel nickel foam-based composite phase change materials for a large-capacity lithium-ion power battery module, *Appl. Therm. Eng.* 236 (2024) 121858, <https://doi.org/10.1016/J.APPLTHERMALENG.2023.121858>.
- [26] H. Yang, G. Zhang, X. Yan, B. Dou, D. Zhang, G. Cui, Q. Yang, Composite phase change materials with carbon foam and fibre combination for efficient battery thermal management: dual modulation roles of interfacial heat transfer, *J. Mater. Res. Technol.* 23 (2023) 551–563, <https://doi.org/10.1016/J.JMRT.2023.01.026>.
- [27] M. Pan, W. Lai, Cutting copper fiber/paraffin composite phase change material discharging experimental study based on heat dissipation capability of Li-ion battery, *Renew. Energy* 114 (2017) 408–422, <https://doi.org/10.1016/J.RENENE.2017.07.004>.
- [28] Q. Deng, Q. Liu, Y. Nian, R. Zhao, W. Cheng, A novel flexible composite phase change material with enhanced toughness and shape stability for battery thermal management, *J. Energy Storage* 72 (2023) 108701, <https://doi.org/10.1016/J.EST.2023.108701>.
- [29] I. Chriaa, A. Trigui, M. Karkri, I. Jedidi, M. Abdelmouleh, C. Boudaya, Thermal properties of shape-stabilized phase change materials based on low density polyethylene, Hexadecane and SEBS for thermal energy storage, *Appl. Therm. Eng.* 171 (2020) 115072, <https://doi.org/10.1016/J.APPLTHERMALENG.2020.115072>.

- [30] Y. Lv, X. Yang, X. Li, G. Zhang, Z. Wang, C. Yang, Experimental study on a novel battery thermal management technology based on low density polyethylene-enhanced composite phase change materials coupled with low fins, *Appl. Energy* 178 (2016) 376–382, <https://doi.org/10.1016/j.apenergy.2016.06.058>.
- [31] J. Wang, Q. Huang, X. Li, G. Zhang, C. Wang, Experimental and numerical simulation investigation on the battery thermal management performance using silicone coupled with phase change material, *J. Energy Storage* 40 (2021) 102810, <https://doi.org/10.1016/j.est.2021.102810>.
- [32] H. Hu, Recent advances of polymeric phase change composites for flexible electronics and thermal energy storage system, *Compos. B Eng.* 195 (2020) 108094, <https://doi.org/10.1016/j.compositesb.2020.108094>.
- [33] A. Palacios, M.E. Navarro-Rivero, B. Zou, Z. Jiang, M.T. Harrison, Y. Ding, A perspective on phase change material encapsulation: guidance for encapsulation design methodology from low to high-temperature thermal energy storage applications, *J. Energy Storage* 72 (2023) 108597, <https://doi.org/10.1016/j.est.2023.108597>.
- [34] P. Venkatakrishnan, P. Palanisamy, A state-of-the-art review on advancements in phase change material encapsulation techniques for electronics cooling, *Phys. Scr.* 98 (2023) 112001, <https://doi.org/10.1088/1402-4896/AD0000>.
- [35] A.A. Minea, Overview of encapsulated phase change materials for thermal runaway control, *Int. J. Thermophys.* 44 (2023) 1–19, <https://doi.org/10.1007/S10765-023-03254-7/FIGURES/4>.
- [36] S. Höhle, A. König-Haagen, D. Brüggemann, A. Koenig, De-Haagen@uni-Bayreuth, D. Brüggemann@uni-Bayreuth, *Macro-Encapsulation of Inorganic Phase-Change Materials (PCM) in Metal Capsules*, *Materials* 2018, Vol. 11, Page 1752 11, 2018, p. 1752, <https://doi.org/10.3390/MA11091752>.
- [37] C. Wickramaratne, J.S. Dhau, R. Kamal, P. Myers, D.Y. Goswami, E. Stefanakos, Macro-encapsulation and characterization of chloride based inorganic phase change materials for high temperature thermal energy storage systems, *Appl. Energy* 221 (2018) 587–596, <https://doi.org/10.1016/j.apenergy.2018.03.146>.
- [38] L. Xu, X. Liu, Z. An, R. Yang, EG-based coatings for flame retardance of shape stabilized phase change materials, *Polym. Degrad. Stab.* 161 (2019) 114–120, <https://doi.org/10.1016/j.polymerdegradstab.2019.01.020>.
- [39] H. Zhang, Q. Dong, J. Lu, Y. Tang, W. Bi, Y. Gao, H. Yang, J. Wang, Modified sodium acetate trihydrate/expanded perlite composite phase change material encapsulated by epoxy resin for radiant floor heating, *J. Energy Storage* 65 (2023) 107374, <https://doi.org/10.1016/j.est.2023.107374>.
- [40] H. Zhang, Q. Dong, Y. Tang, J. Wu, W. Bi, Y. Gao, J. Wang, H. Yang, Sodium acetate trihydrate/melamine foam composite PCM encapsulated by CuS/rGO modified epoxy resin and endowed with light-to-heat conversion properties, *Chem. Eng. J.* 471 (2023) 144462, <https://doi.org/10.1016/j.cej.2023.144462>.
- [41] B. Shang, J. Hu, R. Hu, J. Cheng, X. Luo, Modularized thermal storage unit of metal foam/paraffin composite, *Int. J. Heat Mass Transf.* 125 (2018) 596–603, <https://doi.org/10.1016/j.jlheatmasstransfer.2018.04.117>.
- [42] S. Nishad, Z. Ahmad, I. Krupa, Enhancement of photovoltaic module performance by thermal management using shape-stabilized PCM composites, *Sol. Energy Mater. Sol. Cells* 273 (2024) 112948, <https://doi.org/10.1016/j.solmat.2024.112948>.
- [43] C. Ma, Y. Zhang, S. Hu, X. Liu, S. He, A copper nanoparticle enhanced phase change material with high thermal conductivity and latent heat for battery thermal management, *J. Loss Prev. Process Ind.* 78 (2022) 104814, <https://doi.org/10.1016/j.jlp.2022.104814>.
- [44] J. Weng, D. Ouyang, X. Yang, M. Chen, G. Zhang, J. Wang, Optimization of the internal fin in a phase-change-material module for battery thermal management, *Appl. Therm. Eng.* 167 (2020) 114698, <https://doi.org/10.1016/j.applthermaleng.2019.114698>.
- [45] X. Wu, C. Mo, J. Xie, Y. Xu, X. Yang, G. Zhang, Experimental study of a novel strategy to construct the battery thermal management module by using tubular phase change material units, *J. Energy Storage* 39 (2021) 102585, <https://doi.org/10.1016/j.est.2021.102585>.
- [46] R. Huang, J. Xie, X. Wu, G. Zhang, X. Yang, Preparation of composite cooling boards composed of thermal conductive silica gel and phase change materials for battery thermal management, *Energy Fuel* 35 (2021) 13466–13473, https://doi.org/10.1021/ACS.ENERGYFUELS.1C01966/ASSET/IMAGES/LARGE/EF1C01966_00111.JPEG.
- [47] J.A. Molefi, A.S. Luyt, I. Krupa, Comparison of LDPE, LLDPE and HDPE as matrices for phase change materials based on a soft Fischer–Tropsch paraffin wax, *Thermochim. Acta* 500 (2010) 88–92, <https://doi.org/10.1016/j.tca.2010.01.002>.
- [48] X. Liu, C. Wang, T. Wu, Z. Li, C. Wu, A novel stable and flexible composite phase change materials for battery thermal management, *Appl. Therm. Eng.* 212 (2022) 118510, <https://doi.org/10.1016/j.applthermaleng.2022.118510>.
- [49] Y. Huang, M. Zou, W. Chen, W. Luo, X. Hu, G. Zhu, S. Tan, X. Jiang, A novel room-temperature flexible phase change material for solar energy photothermal conversion and battery thermal management, *ACS Sustain. Chem. Eng.* 12 (2024) 4662–4675, https://doi.org/10.1021/ACSSUSCHEMENG.3C08489/ASSET/IMAGES/LARGE/SC3C08489_0008.JPEG.
- [50] S. Li, X. Dong, X. Lin, D. Shao, G. Zhang, J. Deng, X. Yang, Flexible phase change materials obtained from a simple solvent-evaporation method for battery thermal management, *J. Energy Storage* 44 (2021) 103447, <https://doi.org/10.1016/j.est.2021.103447>.
- [51] X. Yang, G. Deng, Z. Cai, H. Li, J. Zeng, H. Yang, Experimental study on novel composite phase change materials with room-temperature flexibility and high-temperature shape stability in a battery thermal management system, *Int. J. Heat Mass Transf.* 206 (2023) 123953, <https://doi.org/10.1016/j.ljheatmasstransfer.2023.123953>.
- [52] I. Blanco, The use of composite materials in 3D printing, *J. Compos. Sci.* 4 (2020) 42, <https://doi.org/10.3390/JCS4020042>.
- [53] M. Cañado, E. Lizundia, O. Akizu-Gardoki, R. Minguez, B. Lekube, A. Arrillaga, M. Iturrondobetia, 3D printing to enable the reuse of marine plastic waste with reduced environmental impacts, *J. Ind. Ecol.* 26 (2022) 2092–2107, <https://doi.org/10.1111/JIEC.13302>.
- [54] B. Maldonado-García, A.K. Pal, M. Misra, S. Gregori, A.K. Mohanty, Sustainable 3D printed composites from recycled ocean plastics and pyrolyzed soy-hulls: optimization of printing parameters, performance studies and prototypes development, *Compos. Part C: Open Access* 6 (2021), <https://doi.org/10.1016/j.jcomc.2021.100197>.
- [55] R. Alkabbanie, B. Aktas, G. Demircan, S. Yalcin, Short carbon fiber-reinforced PLA composites: influence of 3D-printing parameters on the mechanical and structural properties, *Iran. Polym. J. (Engl. Ed.)* (2024) 1–10, <https://doi.org/10.1007/S13726-024-01315-8/FIGURES/8>.
- [56] A.J. Clarke, A. Dickson, D.P. Dowling, Fabrication and performance of continuous 316 stainless steel fibre-reinforced 3D-printed PLA composites, *Polymers* 16 (2024) 63, <https://doi.org/10.3390/POLYM16010063>.
- [57] J.C. Camargo, Á.R. Machado, E.C. Almeida, E.F.M.S. Silva, Mechanical properties of PLA-graphene filament for FDM 3D printing, *Int. J. Adv. Manuf. Technol.* 103 (2019) 2423–2443, <https://doi.org/10.1007/S00170-019-03532-5/METRCS>.
- [58] T.J. Quill, M.K. Smith, T. Zhou, M.G.S. Baoumy, J.P. Berenguer, B.A. Cola, K. Kalaitzidou, T.L. Bougher, Thermal and mechanical properties of 3D printed boron nitride – ABS composites, *Appl. Compos. Mater.* 25 (2018) 1205–1217, <https://doi.org/10.1007/S10443-017-9661-1/FIGURES/10>.
- [59] K.A. Hamzah, C.K. Yeoh, M.M. Noor, P.L. Teh, Y.Y. Aw, S.A. Szali, W.M.A. Wan Ibrahim, Mechanical properties and thermal and electrical conductivity of 3D printed ABS-copper ferrite composites via 3D printing technique, *J. Thermoplast. Compos. Mater.* 35 (2022) 3–16, https://doi.org/10.1177/0892705719869405/ASSET/IMAGES/LARGE/10.1177_0892705719869405-FIG14.JPEG.
- [60] L. Han, L. Shen, H. Lin, Z. Huang, Y. Xu, R. Li, B. Li, C. Chen, W. Yu, J. Teng, 3D printing titanium dioxide-acrylonitrile-butadiene-styrene (TiO₂-ABS) composite membrane for efficient oil/water separation, *Chemosphere* 315 (2023) 137791, <https://doi.org/10.1016/j.chemosphere.2023.137791>.
- [61] F. Peng, H. Jiang, A. Woods, P. Joo, E.J. Amis, N.S. Zacharia, B.D. Vogt, 3D printing with Core-Shell filaments containing high or low density polyethylene shells, *ACS Appl. Polym. Mater.* 1 (2019) 275–285, https://doi.org/10.1021/ACSAPM.8B00186/ASSET/IMAGES/MEDIUM/AP-2018-00186_M003.GIF.
- [62] M.A. Kreiger, M.L. Mulder, A.G. Glover, J.M. Pearce, Life cycle analysis of distributed recycling of post-consumer high density polyethylene for 3-D printing filament, *J. Clean. Prod.* 70 (2014) 90–96, <https://doi.org/10.1016/j.jclepro.2014.02.009>.
- [63] R. Daniele, D. Armoni, S. Dul, P. Alessandro, From nautical waste to additive manufacturing: sustainable recycling of high-density polyethylene for 3D printing applications, *J. Compos. Sci.* 7 (2023) 320, <https://doi.org/10.3390/JCS7080320>.
- [64] C.G. Schirmeister, T. Hees, E.H. Licht, R. Mühlaupt, 3D printing of high density polyethylene by fused filament fabrication, *Addit. Manuf.* 28 (2019) 152–159, <https://doi.org/10.1016/j.addma.2019.05.003>.
- [65] P. Sobolciak, M. Karkri, M.A. Al-Maadeed, I. Krupa, Thermal characterization of phase change materials based on linear low-density polyethylene, paraffin wax and expanded graphite, *Renew. Energy* 88 (2016) 372–382, <https://doi.org/10.1016/j.renene.2015.11.056>.
- [66] X. Wang, C.P. Feng, M. Wang, H. Lu, H.Y. Ni, J. Chen, Multilayered ultrahigh molecular weight polyethylene/natural graphite/boron nitride composites with enhanced thermal conductivity and electrical insulation by hot compression, *J. Appl. Polym. Sci.* 138 (2021) 49938, <https://doi.org/10.1002/APP.49938>.
- [67] Y. Mamunya, A. Misiura, M. Godzisz, S. Pusz, U. Szeluga, K. Olszowska, P. S. Wróbel, A. Hercog, A. Kobyluk, A. Pylypenko, Polymer Composites with Carbon Fillers Based on Coal Pitch and Petroleum Pitch Cokes: Structure, Electrical, Thermal, and Mechanical Properties, *Polymers* 2024, Vol. 16, Page 741 16, 2024, p. 741, <https://doi.org/10.3390/POLYM16060741>.
- [68] S. Shi, W. Xu, B. Zhou, S. Qin, X. Liu, H. Li, Low-density polyethylene-multi-walled carbon nanotube nanocomposite membranes with enhanced conductivity for highly sensitive vapor sensing, *Adv. Compos. Hybrid Mater.* 6 (2023) 1–12, <https://doi.org/10.1007/S42114-023-00748-8/FIGURES/5>.
- [69] Y. Wang, W. Zhang, M. Feng, M. Qu, Z. Cai, G. Yang, Y. Pan, C. Liu, C. Shen, X. Liu, The influence of boron nitride shape and size on thermal conductivity, rheological and passive cooling properties of polyethylene composites, *Compos. Part A Appl. Sci. Manuf.* 161 (2022) 107117, <https://doi.org/10.1016/j.compositesa.2022.107117>.
- [70] X. Zhou, J. Yang, Z. Gu, Y. Wei, G. Li, C. Hao, Q. Lei, Effect of boron nitride concentration and morphology on dielectric and breakdown properties of cross-linked polyethylene/boron nitride nanocomposites, *Adv. Eng. Mater.* 23 (2021) 2100008, <https://doi.org/10.1002/ADEM.202100008>.
- [71] Y. Shang, G. Yang, F. Su, Y. Feng, Y. Ji, D. Liu, R. Yin, C. Liu, C. Shen, Multilayer polyethylene/ hexagonal boron nitride composites showing high neutron shielding efficiency and thermal conductivity, *Compos. Commun.* 19 (2020) 147–153, <https://doi.org/10.1016/j.cocom.2020.03.007>.
- [72] S. Kumar, M.R. Ramesh, M. Doddamani, S.M. Rangappa, S. Siengchin, Mechanical characterization of 3D printed MWCNTs/HDPE nanocomposites, *Polym. Test.* 114 (2022), <https://doi.org/10.1016/j.polymertesting.2022.107703>.
- [73] W.N.W. Busu, R.S. Chen, M.J. Mohd Yusof, S. Ahmad, Graphene enhanced linear low-density polyethylene nanocomposites by premixing and melt compounding, *J. Met. Mater. Miner.* 31 (2021) 11–16, <https://doi.org/10.14456/JMMM.2021.2>.

- [74] B. Shang, J. Hu, R. Hu, J. Cheng, X. Luo, Modularized thermal storage unit of metal foam/paraffin composite, *Int. J. Heat Mass Transf.* 125 (2018) 596–603, <https://doi.org/10.1016/J.IJHEATMASSTRANSFER.2018.04.117>.
- [75] D. Zhang, J. Zhou, K. Wu, Z. Li, Granular phase changing composites for thermal energy storage, *Sol. Energy* 78 (2005) 471–480, <https://doi.org/10.1016/J.SOLENER.2004.04.022>.
- [76] L. Xia, P. Zhang, R.Z. Wang, Preparation and thermal characterization of expanded graphite/paraffin composite phase change material, *Carbon N Y* 48 (2010) 2538–2548, <https://doi.org/10.1016/J.CARBON.2010.03.030>.
- [77] S. Nishad, M. Ouederni, I. Krupa, Thermal energy storage materials designed from recycled Tetra Pak waste and paraffin waxes with enhanced photothermal conversion efficiencies, *Energ. Built Environ.* (2024), <https://doi.org/10.1016/J.ENBENV.2024.01.003>.
- [78] Standard Test Method for Steady-State Thermal Transmission Properties by Means of the Heat Flow Meter Apparatus, (n.d.). <https://www.astm.org/standards/c518> (accessed April 24, 2022).
- [79] G. Zhang, Y. Sun, C. Wu, X. Yan, W. Zhao, C. Peng, Low-cost and highly thermally conductive lauric acid–paraffin–expanded graphite multifunctional composite phase change materials for quenching thermal runaway of lithium-ion battery, *Energy Rep.* 9 (2023) 2538–2547, <https://doi.org/10.1016/J.EGYR.2023.01.102>.
- [80] G. Jiang, J. Huang, Y. Fu, M. Cao, M. Liu, Thermal optimization of composite phase change material/expanded graphite for Li-ion battery thermal management, *Appl. Therm. Eng.* 108 (2016) 1119–1125, <https://doi.org/10.1016/J.APPLTHERMALENG.2016.07.197>.
- [81] W. Yang, X. Li, C. Li, J. Deng, Y. Du, G. Zhang, High Antileakage and thermal conductivity composite phase-change material with anisotropy expanded graphite for battery thermal management, *ACS Appl. Energy Mater.* 6 (2023) 9698–9708, https://doi.org/10.1021/ACSAEM.3C01819/ASSET/IMAGES/LARGE/AE3C01819_0009.JPEG.
- [82] Y. Wang, L. Zhao, W. Zhan, Y. Chen, M. Chen, Flame retardant composite phase change materials with MXene for lithium-ion battery thermal management systems, *J. Energy Storage* 86 (2024) 111293, <https://doi.org/10.1016/J.EST.2024.111293>.
- [83] W. Yang, R. Lin, X. Li, C. Li, Y. Wu, G. Zhang, X. Liu, S. Li, Y. Wang, High thermal conductive and anti-leakage composite phase change material with halloysite nanotube for battery thermal management system, *J. Energy Storage* 66 (2023) 107372, <https://doi.org/10.1016/J.EST.2023.107372>.
- [84] X. Liu, C. Wang, T. Wu, Z. Li, C. Wu, A novel stable and flexible composite phase change materials for battery thermal management, *Appl. Therm. Eng.* 212 (2022) 118510, <https://doi.org/10.1016/J.APPLTHERMALENG.2022.118510>.
- [85] Z. Ling, S. Li, C. Cai, S. Lin, X. Fang, Z. Zhang, Battery thermal management based on multiscale encapsulated inorganic phase change material of high stability, *Appl. Therm. Eng.* 193 (2021) 117002, <https://doi.org/10.1016/J.APPLTHERMALENG.2021.117002>.
- [86] X. Lin, X. Zhang, J. Ji, L. Liu, M. Yang, L. Zou, Experimental investigation of form-stable phase change material with enhanced thermal conductivity and thermal-induced flexibility for thermal management, *Appl. Therm. Eng.* 201 (2022) 117762, <https://doi.org/10.1016/J.APPLTHERMALENG.2021.117762>.
- [87] S. Cai, J. Ji, X. Zhang, C. Zhang, Z. Pan, C. Zhang, Y. Zhao, Development of bio-based flexible phase change materials utilizing lauric acid for battery thermal management systems, *J. Energy Storage* 86 (2024) 111382, <https://doi.org/10.1016/J.EST.2024.111382>.
- [88] Y. Ma, M. Zou, W. Chen, W. Luo, X. Hu, S. Xiao, L. Luo, X. Jiang, Q. Li, A structured phase change material integrated by MXene/AgNWs modified dual-network and polyethylene glycol for energy storage and thermal management, *Appl. Energy* 349 (2023) 121658, <https://doi.org/10.1016/J.APENERGY.2023.121658>.